LUND UNIVERSITY

Large screen enabled tri-port MIMO handset antenna for low LTE bands

Aliakbari Abar, Hanieh; Nie, Li Ying; Lau, Buon Kiong

Large Screen Enabled Tri-port MIMO Handset Antenna for Low LTE Bands

Hanieh Aliakbari, *Graduate Student Member, IEEE,* Li Ying Nie, and Buon Kiong Lau, *Senior Member, IEEE*

Abstract In recent years, the screen-to-body ratio of mobile handsets has been increasing. Today, the screen nearly fills up the entire front side. Conventionally, the screen is mainly seen as a metallic object that adversely affects antenna performance. In this paper, the large screen is used for the first time to facilitate an additional uncorrelated MIMO port in a tri-port design, for several LTE bands below 1 GHz. To this end, the screen and the terminal chassis are modeled as two metal plates and their characteristic modes are analyzed. Four modes are then tuned to resonance and selectively excited to yield three uncorrelated MIMO ports. Simulation and measurement results are in good agreement. The measured bandwidths are 23%, 17% and 21%. Within the operating band, the measured isolation is above 13 dB, envelope correlation coefficient below 0.16 and average total efficiency above 72%.

Index Terms— **Characteristic mode analysis, handset antenna, MIMO systems, mobile antenna, mutual coupling.**

I. INTRODUCTION

ONE key technology for increasing the channel capacity (ideal data rate) of wireless communication systems is multiple-input multiple-output (MIMO) system. The capacity of a MIMO system is closely related to the number of the antenna elements, as well as the antenna efficiencies and the correlation of signals among these antennas.

Many MIMO terminal antennas with more than two ports have been proposed for sub-6 GHz cellular bands in recent years. However, most of these multiport antenna systems are designed for frequencies above 1.71 GHz (i.e., conventional "high bands") [1]-[3]. The popularity with high band designs is not only because MIMO was first deployed on a massive scale in the LTE band around 2.6 GHz. More importantly, it is technically very challenging to design MIMO antenna with high efficiency and low correlation for cellular bands below 1 GHz, e.g., LTE Band 5 (0.824-0.894 GHz). The reason is that such low-band antennas rely on the entire chassis for radiation and large bandwidth, and generally the electrically compact chassis with only one resonant mode (dipole mode along chassis length) cannot support low coupling and correlation desired for multiport MIMO operation [4]. For example, the quad-element design in [5] is only intended for dual-port MIMO operation by antenna selection. Moreover, the isolation in

the 0.75-0.96 GHz band is only above 6 dB and the envelope correlation coefficient (ECC) is as high as 0.75.

Nonetheless, dual-port MIMO antennas with moderate to low coupling/correlation have been successfully designed for frequency bands below 1 GHz [4], [6]-[12], either by having a second self-resonant narrowband antenna that does not radiate through the chassis [4], [6] or facilitating a second resonant mode by making use of minor changes in the chassis [7]-[12]. The minor changes include the use of loading strips [7], [8] and a bezel frame [9]-[11], some in combination with a larger chassis width (~80 mm) [10]-[12].

Recently, a tri-port MIMO antenna with low correlation has been designed for these frequencies [13]. However, the focus of [13] is to significantly extend the bandwidth of the previous dual-port design in [7] from 9% to 25%. The addition of the third port is mainly to show that a well-isolated tri-port antenna can be achieved by placing one magnetic antenna at the top end of the chassis. However, since the magnetic antenna does not rely on the chassis for radiation, its bandwidth is only around 2%, and tuning is needed to cover the operating band [13]. Therefore, the challenge is to find a tri-port solution with sufficient isolation and bandwidth over all three ports, without the need for frequency tuning [13] or decoupling structures [12]. Importantly, a tri-port antenna can offer 50% higher data rate than a two-port antenna in MIMO operation, if the correlation is low among the ports.

Hanieh Aliakbari and Buon Kiong Lau are with the Department of Electrical and Information Technology, Lund University, 221 00 Lund, Sweden (E-mail: buon_kiong.lau@eit.lth.se).

Li Ying Nie is with the School of Computer Science and Information Engineering, Hefei University of Technology, Hefei 230601, China (E-mail: liyingnie@sina.com).
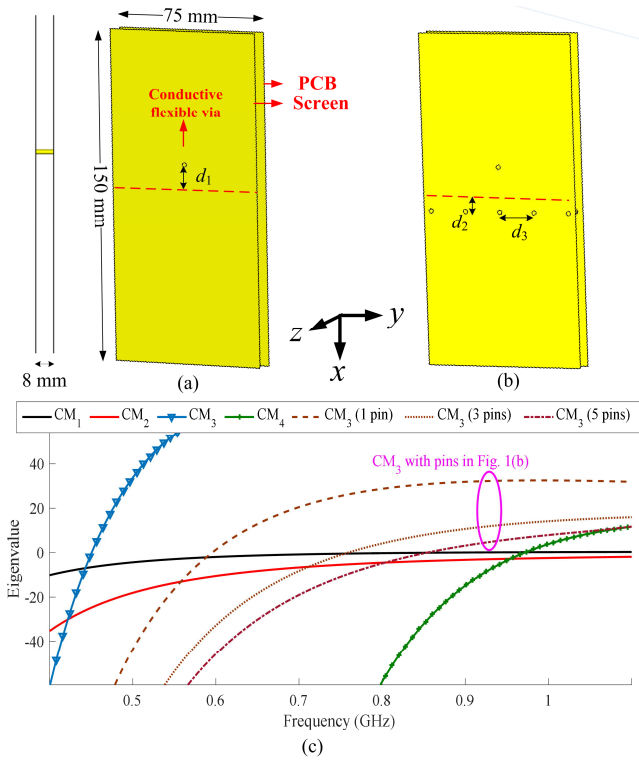
Fig. 1. (a) Geometry and parameters of the connected metal plates ($d_1 = 15$ mm), (b) geometry with 5-metal pins added ($d_2 = 5$ mm, $d_3 = 17$ mm), and (c) Eigenvalues of the modes of interest for the dual-plate model with and without pins.

Increasing the screen-to-body ratio of smartphones is an ongoing trend, with it growing from 30.1% to 93.8% over the last 12 years [14], [15]. As a result, the screen covers nearly the entire front side, except for a few millimeters at the sides [16]. The screen is metal covered to enhance its structural strength [16]. In [1], the screen is modeled with only a dielectric plate (i.e., glass with a relative permittivity of 5.5). Hence, it has a limited influence on the antenna performance in the 3.5 GHz 5G band. As a more accurate model, a copper layer has been used to model the screen [17]. However, the screen-to-body ratio is small (45%) and the effect of the screen is less prominent. To the best of the authors' knowledge, there are very few literatures on smartphone antenna design that explicitly model the large metal-covered screen in the design procedure [16], [18].

The effect of the large metal-covered screen was studied in [16] for a metal-framed monopole antenna or a planar inverted-F antenna (PIFA) mounted on the top end. The screen, which in practice is grounded to the terminal chassis, was found to severely degrade the bandwidth. In [18], the study of metal-covered screen is extended to design a multi-band single-port antenna, covering several LTE and 5G bands. Specifically, characteristic mode analysis (CMA) [19] was used to address the bandwidth degradation effect of the large screen observed in [16]. This is because the screen can be included in the design procedure through CMA, and the bandwidth impact can be mitigated by selectively exciting and merging as many resonant characteristic modes (CMs) as possible. However,

no effort has so far been made to take advantage of the metal-covered screen to enable one more antenna port with a relatively large bandwidth, relative to the no-screen chassis model used for antenna design.

In this paper, the large screen is explicitly utilized by CMA to enable the design of a tri-port MIMO antenna below 1 GHz. The design procedure is based on two new resonant modes generated by the addition of the large screen, which facilitates the increase of the number of CMs (per frequency) in [7] from two to four. These two modes were then jointly and selectively excited by port 1 to improve bandwidth and correlation performances, respectively. Differential feeding is used by port 2 to avoid exciting the new modes, which is different from the single-feed design in [7]. Finally, the dipole mode along the chassis length is selectively excited by port 3 by adding a shorting pin to connect between the top end of the screen and the PCB. The proposed design concept yields at least 17% bandwidth for the tri-port antenna, showing that a tri-port design is feasible from both bandwidth and correlation perspectives even for MIMO operation below 1 GHz. Furthermore, as mentioned above, the tri-port design with low ECC (<0.16) can ideally offer 50% higher data rate for 3×3 MIMO, relative to a dual-port design for 2×2 MIMO.

II. LARGE-SCREEN INDUCED MODES AND SINGLE-PORT EXCITATION

A. CMA of Connected Double-Plate Model

For a large-screen smartphone, the entire metal chassis is more accurately modelled as two connected parallel metal plates, i.e., the screen and the printed circuit board (PCB) (see Fig. 1(a)). As shown in the smartphone model in Fig. 1(a), there is normally a conductive flexible via (represented by a conductive pin of 1 mm in diameter, located d_1 above the center of each plate) that connects the screen assembly to the PCB [16]. The total model size is $150 \times 75 \times 8$ mm^3, which can be considered typical for smartphones (e.g., Samsung S9 [15]). The addition of a large parallel plate to the single-PCB model is expected to significantly change the CMs of the chassis structure.

In this section, CMA is performed using 2018 Altair FEKO to explore the available modes in this connected double-plate chassis, assumed to be a perfect electric conductor (PEC). For the initial analysis, the screen size is set to be the same as the PCB size (see Fig. 1(a)). As also found in [18] for slightly different plate sizes, the new structure of the smartphone chassis will bring different and new resonating CMs in comparison with a single PEC plate of the same dimension (see Fig. 1(c)). The first mode (CM$_1$) in Fig. 1(c) is the longitudinal half wavelength (0.5λ) dipole mode and the second one (CM$_2$) is the transversal 0.5λ-dipole mode, both of which also exist in single-PCB models. The lowest-order mode (CM$_3$) is a monopole-like mode that is due to two connected plates and the fourth mode (CM$_4$) is a patch-like mode due to adding the screen at the distance of h to the PCB ($h = 8$ mm in Fig. 1(a)). The
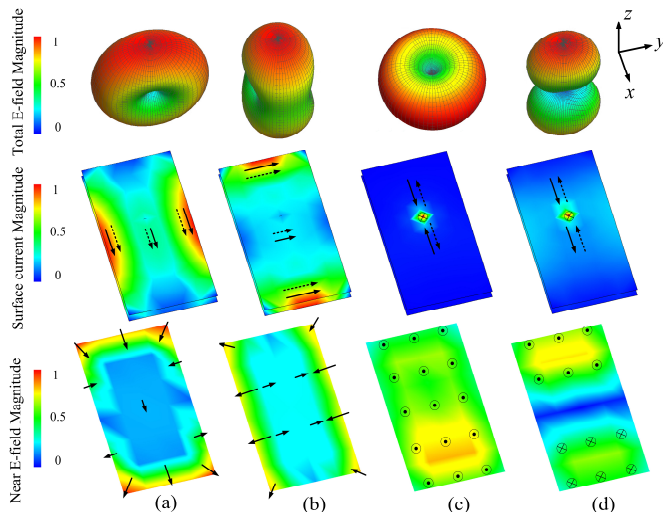
Fig. 2. The normalized far-field patterns, surface currents on the two plates and electric near-field in between two plates for (a) CM_1, (b) CM_2, (c) CM_3, and (d) CM_4 at their respective resonance frequencies. "$\odot$" and "$\otimes$" represent E-field/current in positive and negative z directions, respectively. Solid and dashed arrows show the currents on the screen and PCB, respectively.

Fig. 3. (a) Modal weighting coefficient of the modes of interest for P_1 excitation, (b) S_{11} before matching for different parameters (d_3, h).

Fig. 4. (a) Prototype of the single-port antenna, (b) measured and simulated S_{11}.

parameter h has little effect on the resonant frequency of CM_1 and CM_2 in Fig. 1(c).

The characteristic far-field patterns, surface current distributions and electric field (E-field) distribution half-way between the two plates are shown for CM_1-CM_4 in Fig. 2. For CM_3, the surface currents on the screen flow into the metallic pin and then exit the pin into the PCB. The directions of the currents are reversed on the two plates and the currents reach a maximum value on the conductive flexible via (pin). The characteristic E-field of CM_3 is almost consistently in the positive z-direction in the volume between the plates. In contrast, the E-field for CM_4 is in both positive (top half) and negative (bottom half) z-directions, with a minimum E-field magnitude at the middle line. Depending on the position of the conductive flexible via (i.e., d_1 in Fig. 1(a)), the position of the minimum near E-field line of CM_4 can depart from the center. Moreover, the currents for CM_4 are in the same direction over the entire screen, whereas they flow in the opposite direction over the entire PCB. But like CM_3, the currents are maximum along the via. Contrary to CM_3 and CM_4, the directions of the surface currents are the same on the two plates for CM_1 and CM_2, and the current is minimum on the conductive flexible via. Moreover, the E-field direction between the plates is in the xy-plane for CM_1 and CM_2.

As shown in Fig. 1(c), the resonance of CM_3 in the initial structure (i.e., 452 MHz) is lower than the desired operating frequency range (~0.8-1.0 GHz). According to [20], when a circular patch (i.e., two parallel circular plates) is not shorted with a pin, the resonant frequency for the lowest order mode (i.e., TM_{01} or monopole mode in a circular patch antenna) is zero. To increase the modal resonant frequency, shorting pins were introduced to shorten the current paths [20]. Similarly, shorting pins can be added between the two plates in the initial structure (see Fig. 1(a))
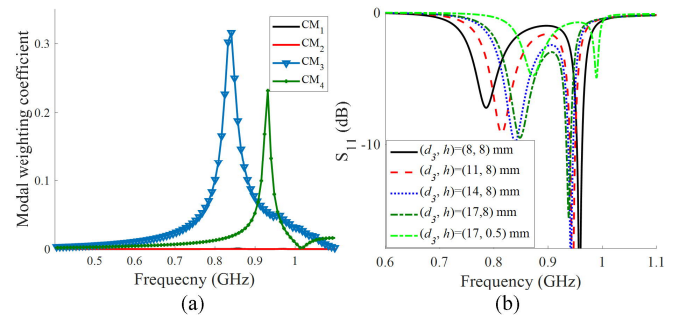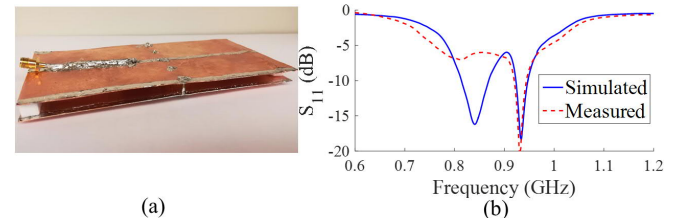
to increase CM_3's resonant frequency, resulting in the structure depicted in Fig. 1(b). As shown in Fig. 1(c), as the number of pins increases, the resonant frequency of CM_3 increases. However, the resonances of CM_1 and CM_2 remain unchanged, mainly due to their E-fields not being in the z-direction. To minimize any influence from the pins on the resonance of CM_4, the pins should be positioned along the line of minimum E-field magnitude for CM_4. As mentioned earlier, the minimum E-field region of CM_4 depends on d_1 and it can be moved downward from the middle if d_1 increases. Thus, d_1 and d_2 were optimized to tune the resonant frequencies of both CM_3 and CM_4 to the desired band. The result is that $d_1 = 15$ mm and $d_2 = 5$ mm for the 5-pin case.

B. Excitation of new CMs by the 1st Port

Having tuned the resonances of CM_3 and CM_4 to the desired band, the next step is to design the feed to simultaneously excite these two modes to achieve a wideband dual-resonance, for the 5-pin model. By comparing the characteristic currents and E-fields of modes with small eigenvalues within the desired frequency range (0.8-1.0 GHz) in Fig. 1(c), it can be seen that the currents of CM_3 and CM_4 have similar behavior along the via (i.e., maximum and in the same negative z-direction). So, a single feed at that location should be able to excite both CM_3 and CM_4, giving dual-resonance. Moreover, this single feed should not excite either CM_1 or CM_2, as their currents are very small along the via (see Figs. 2(a) and 2(b)). The selective excitation of CM_3 and CM_4 was verified using the modal weighting coefficients for this port (P_1) (see Fig. 3(a)). This strategy also allows CM_1 and CM_2 to be used for other ports, and low correlation with other ports is guaranteed as long as they do not excite CM_3 and CM_4.
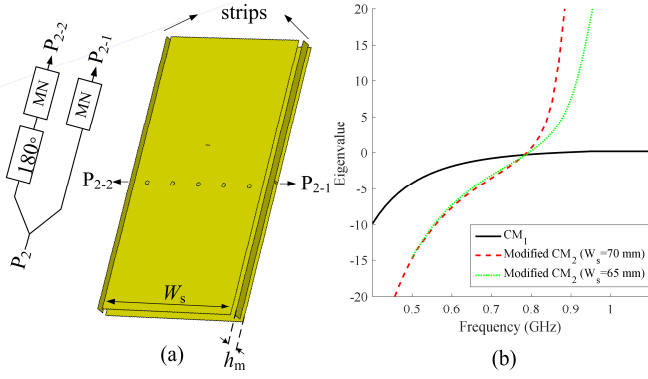
Fig. 5. (a) Connected plates with metal strips and the feeding network consisting of a power divider with a 180° phase difference in the output ports and matching networks (MN) (W_s = 70 mm, h_m = 7 mm), (b) modified eigenvalue for different screen sizes.
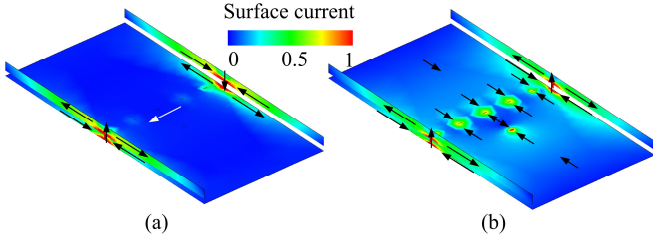

Fig. 6. Modified surface currents by adding two grounded loading strips for (a) CM_2, and (b) CM_3. For clarity, the screen and connecting pins are not shown.
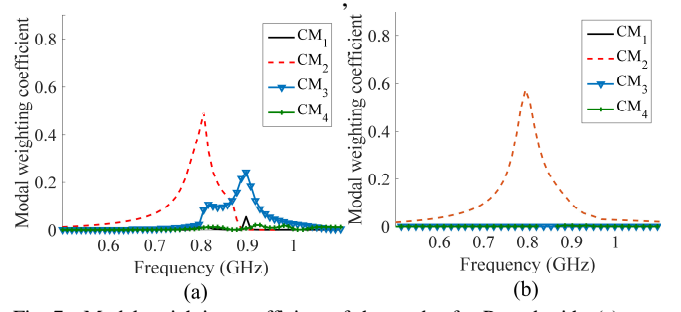

Fig. 7. Modal weighting coefficient of the modes for P_2 and with: (a) one feed, and (b) two feeds with 180° phase shift (W_s = 70 mm). The feed power is kept equal in both cases.

As shown in Fig. 3(b), as the distance between the pins (i.e., d_3) increases, the resonant frequency of CM_3 increases and that of CM_4 remains almost unchanged. The latter is due to the pins being in a region of low E-field for CM_4. Finally, both modes were matched using a three-element ∏ matching network consisting of a 3.9 pF series capacitor, as well as 19.8 nH and 14 nH parallel inductors. It is noted that the number of elements and configuration of the matching networks for achieving the maximum bandwidth potential [21] were found using BetaMatch [22]. To validate this new concept, the optimized single-port antenna was fabricated and shown in Fig. 4(a). A 20% bandwidth (792-968 MHz) is achieved with this matching network (see Fig. 4(b)). The measured $|S_{11}|$ in Fig. 4(b) is slightly different from the simulated ones, but it still covers the targeted band. This discrepancy is mainly due to imperfect Murata matching component modeling, imperfect soldering, and component aging.

Moreover, even if the gap between two plates model is drastically decreased, e.g., to h = 0.5 mm, to account for very extremely small gaps (in reality, the components between the layers should result in larger gaps), the two targeted modes (i.e., CM_3 and CM_4) are still present. These modes can still be used to provide an orthogonal third port for the given h with suitable tuning. Specifically, the resonant frequency of CM_3 can be lowered by decreasing d_3, whereas the resonant frequency of CM_4 can be tuned by a small increase in the chassis size, and its excitation can be modified by increasing d_1 and d_2. For this extreme case, the bandwidth (with matching) is 8% and the average radiation efficiency is 78% in the operating band.

III. ANALYSIS AND EXCITATION OF OTHER RESONANT MODES

In principle, the remaining tasks in designing the proposed tri-port MIMO antenna are to ensure that CM_1 and CM_2, are selectively excited by P_2 and P_3. In particular, the port design for CM_1 and CM_2 must also avoid exciting CM_3 and CM_4, which are used by P_1.

A. Tuning and Selective Excitation of CM_2 by the 2nd Port

For the connected double-plate chassis, CM_2 has a transversal 0.5λ-dipole far-field pattern (see Fig. 2(b)) and a resonant frequency well above 1 GHz (see Fig. 1(c)). To reduce the resonant frequency to below 1 GHz, the structure can be capacitive loaded along the longer sides of the PCB plate with two center-grounded 150 mm × 5 mm metal strips (see Fig. 5(a)). The strips are placed 3 mm above the sides. This modification lowers the resonant frequency of CM_2 with respect to Fig. 1(c). Moreover, it can be seen in Fig. 5(b) that as the clearance between the screen and the strips is increased, the slope of the eigenvalue of CM_2 decreases. Thus, to ensure that the bandwidth potential [21] of port 2 (P_2) is acceptable, the screen width W_s is reduced from 75 mm to 70 mm. With these structure modifications, the far-field pattern of each mode remains the same as that of the original double-plate structure (see Fig. 2). However, the characteristic currents are slightly modified due to the two loading strips. For instance, the modified currents of CM_2 and CM_3 are illustrated in Figs. 6(a) and 6(b), respectively. To study the impact of full metal frame, two metal strips were added to the top and bottom edges, with small gaps (e.g., 3 mm) to the metal strips along longer sides. This addition was found to have limited impact on the utilized modes or their excitation using the existing feed structure.

To excite CM_2, the feeding port can be placed at a high-current location. One such location is any one of the two shorting pins for the loading strips, as can be seen in Fig. 6(a). Through replacing one of the two shorting pins with a gap feed port, the modal weighting coefficient is calculated and plotted in Fig. 7(a). It can be seen that, by adding one feed, CM_2 will be excited. Moreover, the center location of the feed along the strip helps to prevent the excitation of CM_1 and CM_4 due to their low E-fields at this location, as
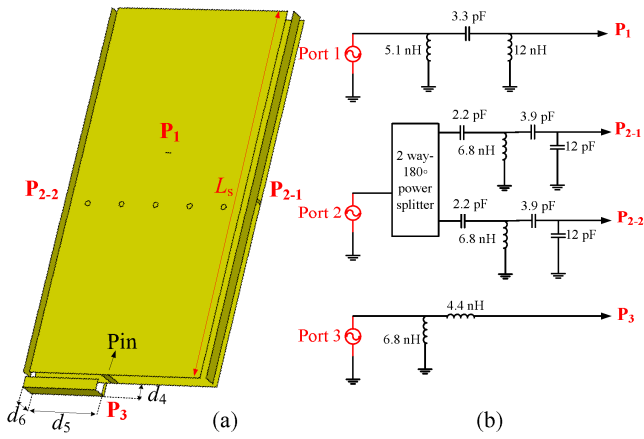
Fig. 8. (a) Antenna structure with one CCE (d_4 = 5 mm, d_5 = 30 mm, d_6 = 6 mm, L_s = 145 mm), (b) matching networks consisting of components connected to the ports.
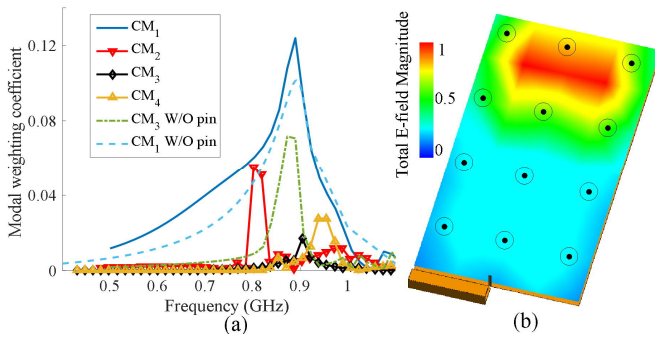

Fig. 9. (a) Modal weighting coefficient of the modes for P_3 and, (b) electric near-field of the CM_3 mode (half-way between the screen and the PCB) after adding a shorting pin close to the single CCE.

shown in Figs. 2(a) and 2(d). Nonetheless, as shown in Fig. 7(a), CM_3 has also been excited by this feed, as it has high current at those locations, as shown in Fig. 6(b).

To selectively excite CM_2, the currents of CM_2 and CM_3 (in Figs. 6(a) and 6(b), respectively) were compared. As can be seen, although the currents on the shorting pins (of the metal strips) flow in different directions for CM_2 they are in the same direction for CM_3. Thus, instead of exciting CM_2 with only one feed, the other pin is also replaced with a feed, with a new port (P_2) feeding them with a 180° phase difference to ensure no excitation of CM_3 (see Fig. 5(a)). The resulting modal weighting coefficient in Fig. 7(b) reveals that CM_3 is no longer excited with this differential feeding scheme. This kind of selective feeding for P_2 is different from feeding in [6], in which a single coupling element connected to one of the strips has been used.

Each of the ports in Fig. 5(a) was matched in BetaMatch [22] (see Fig. 8(b)), which yields a 6 dB impedance bandwidth of 15% (830-960 MHz) as depicted in Fig. 11. It is noted that, as the width of the screen W_s decreases, the number of elements needed to match the loading strip port (P_2) is smaller. In addition, as the distance of the screen to the PCB h together with the strip height (h_m) increases, the impedance bandwidth of the port improves.

B. Tuning and Selective Excitation of CM_1 by the 3rd Port

Considering the E-field distribution of CM_1 in Fig. 2(a), it is common to use one capacitive coupling element (CCE) at a corner of the PCB to excite this mode [23]. To keep the overall length of the structure constant at 150 mm upon adding the CCE, the length of the double-plate model is reduced by d_4 (i.e., ground clearance in Fig. 8(a)). In practice, d_4 should be optimized based on the required ground clearance and achievable bandwidth [23]. Multiple CCEs or more matching elements can be used to reduce the clearance for a given targeted bandwidth. The modal weighting coefficients of CM_1-CM_4 for a single CCE utilized as the third port are shown in Fig. 9(a). It can be seen in Fig. 9(a) that CM_3 is also excited by the CCE, whereas other modes are only slightly excited in the band of interest.

To remedy this problem, a shorting pin was added between the screen and the PCB at the top center position, near the position of the CCE. This solution was motivated by the E-field behavior seen in Fig. 2, i.e., the E-field of CM_3 is z-oriented whereas that of CM_1 is oriented along the xy-plane. Therefore, the added pin shorted out the E-field of CM_3 in this region (see Fig. 9(b)), without affecting that of CM_1, such that the excitation of CM_3 notably decreased, as shown in Fig. 9(a). To match the CCE for P_3, a two-element L matching network with two inductors was used, resulting in the 6 dB bandwidth of 790-960 MHz, as shown in Fig. 11. If the length of the screen L_s is increased beyond 145 mm, the bandwidth of this port will be reduced [16]. Thus, for the final configuration shown in Fig. 8(a), the screen to body ratio is ~90%.

It is noted that only one CCE is used to excite CM_1 (see Fig. 8(a)), to achieve a compact implementation and allow for more space for possible higher band antennas. It was shown that if the number of properly phased and positioned CCEs (for CM_1) is increased, the complexity of the matching network to achieve a certain bandwidth decreases [23]. Furthermore, multiple CCEs will facilitate more selective excitation of CM_1, reducing coupling with the other ports.

IV. EXPERIMENTAL RESULTS

To validate the proposed design concept, a prototype of the tri-port antenna was fabricated (see Fig. 10). Two 0.3mm thick copper plates were used to implement the PCB and the screen. The feeding networks were etched on a 0.25 mm Rogers 4350 substrate with the relative permittivity of 3.48. To excite the two strips from the middle with the same magnitude and 180° phase difference, a surface mount 2 way-180° power splitter (Mini-circuits SYPJ-2-222+) was used. To ease the implementation of the feeding network, a substrate is attached on the bottom side of the PCB by using a conductive glue. Alternatively, the network can also be placed between the two plates (see Fig. 14(b)). It is noted that the simple feeding networks in Fig. 10 are only
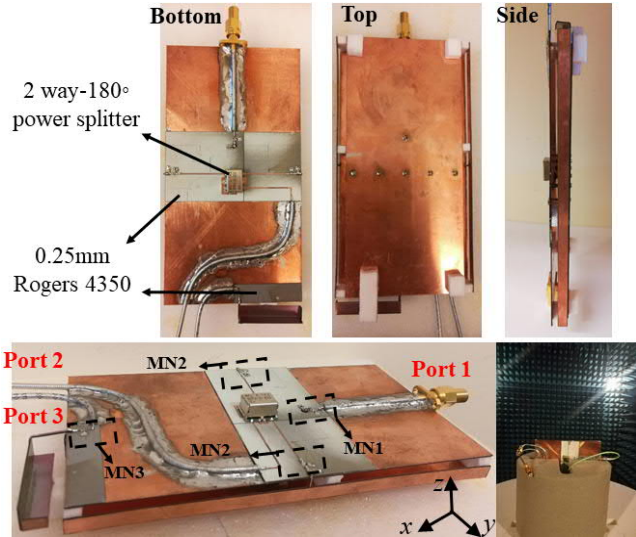
Fig. 10. Prototype of the proposed tri-port MIMO antenna shown with different viewing angles, and it being mounted for pattern measurement (bottom right).

Fig. 11. Simulated (S) and measured (M) S-parameters of the tri-port antenna.

Fig. 12. Measured radiation patterns of (a) P_1, (b) P_2, and (c) P_3 in xy (solid)- and yz (dashed)-planes at 0.9 GHz, individually normalized at each port.

Fig. 13. Simulated ((S), (OH), (TH)) and measured (M) ECC of the tri-port antenna.

intended to verify the operation of the proposed tri-port antenna. In real implementation, the power splitter and matching elements should be realized with integrated circuits and optimized with respect to the active RF circuitry, to minimize any possible interference. The proposed feeding network in Fig. 10 can be implemented in any advanced multilayer technology, which isolates it from the components between the plates.

Figure 11 shows the simulated and measured S-parameters of the proposed tri-port antenna. S_{13} and S_{23} are higher than S_{12}, since the CCE of P_3 will partially excite the other modes, as illustrated earlier in Fig. 9(a). Nevertheless, the measured isolation is over 13 dB, 20 dB, 17 dB for S_{13}, S_{12} and S_{23}, respectively, which are considered as low enough in terminal applications for frequencies below 1 GHz (e.g., [4]-[13]). The relatively high isolation among the ports was achieved by creating multiple resonant CMs in the low band and selectively exciting them. In contrast, traditional low-band handsets mostly benefit from only one resonant mode (CM_3). The 6 dB impedance bandwidth of P_1, P_2 and P_3 are 23% (0.79-1 GHz), 17% (0.82-0.98 GHz) and 21% (0.8-0.98 GHz), respectively. Good agreement is observed between the simulated and measured bandwidths. The measured S_{11} and S_{22} have slightly larger bandwidths than the simulated ones, but the in-band matching is slightly worse. S_{33} is slightly shifted at higher frequencies, but it still covers the targeted band. The discrepancies are mainly due to small differences between the nominal and actual values of the Murata components. The nominal values were used in the simulations.

It is further noted that the $|S_{11}|$ result in Fig. 11 is slightly different from that of Fig. 4, even though the same modes are excited. This is because the final prototype of Fig. 8 must be modified from the single-port variant, as described in Section III, to allow for additional modes to be created and selectively excited by two further ports (i.e., P_2 and P_3).
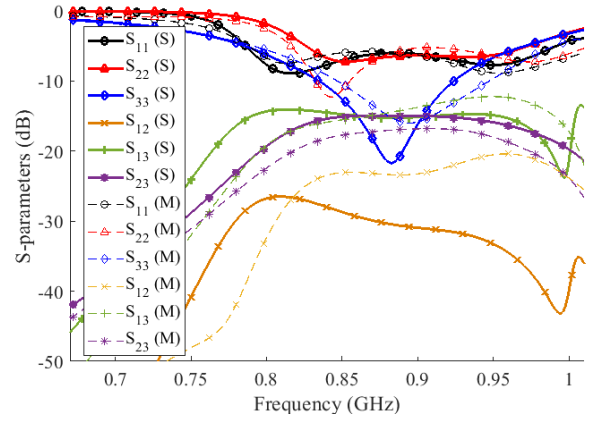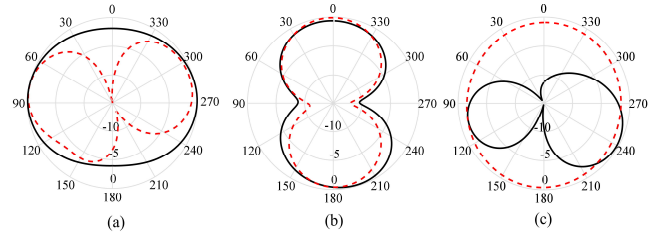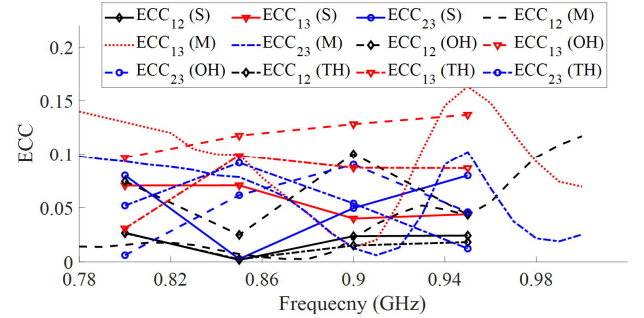
The radiation parameters of the fabricated prototype were obtained from a SATIMO multi-probe spherical near-field system in an anechoic chamber [24]. As expected, it can be observed in Fig. 12 that the total radiation patterns of P_1-P_3 at 0.9 GHz are very similar to the far-field patterns of CM_3, CM_2, and CM_1, respectively (see Fig. 2), since each port was designed to selectively excite one of these modes. The contribution from CM_4 to the pattern of P_1 only becomes more prominent at higher frequencies, as it contributes to the second/higher resonance of P_1. The minor differences between the radiation patterns of the fabricated prototype and those of the CMs are primarily due to the presence of a feeding cable, connected to one of the three SMA connectors on the prototype, which was in the near field of the structure. Other reasons for the minor differences include tolerances in the fabrication and possible small phase/amplitude imbalances of the power splitter used.

The ECC, as calculated from the measured patterns [25], [26], is below 0.16 for all three ports (see Fig. 13).
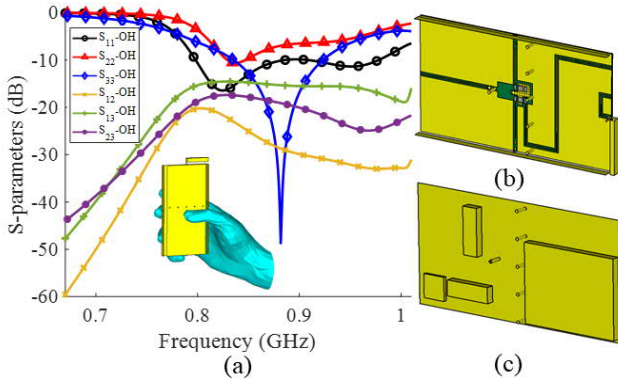
Fig. 14. (a) Simulated S-parameters of the tri-port antenna in one hand (OH) mode. (b) model with CPW feeding network inside the gap. The screen is not shown for clarity; (c) layout of the antenna in a semi-populated handset device.
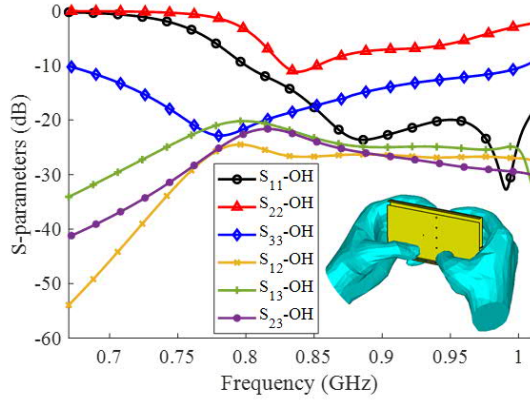

Fig. 15. Simulated S-parameters of the tri-port antenna in two hand (TH) mode.

Simulated and measured ECCs in Fig. 13 were evaluated using a program implemented in MATLAB and antenna correlation tool in the SATIMO software, respectively. The average measured total efficiencies of P_1-P_3 in their operating bandwidths are 74%, 72%, and 80%, respectively. The total efficiencies of the three ports are over 70% in the common bandwidth (0.82-0.98 GHz). The efficiency values were obtained from the radiation patterns measured using the SATIMO system [24].

The efficiency values are affected by the losses of the power splitters and the feeding networks. The coaxial cables in Fig. 10 were only added for experimental verification of the tri-port antenna design. They were well soldered to the chassis to mitigate cable influence. Coplanar waveguides (CPWs), more suitable for integrated circuits, should be used instead of all the transmission lines (TLs) in practice (Fig.14 (b)). However, the antenna performance was found to be similar for different types of TLs, due to the relatively low operating frequency.

To provide more insight into the system performance and the respective contributions from the total efficiencies and ECCs of the three ports, multiplexing efficiency [27] is used. Essentially, it is an equivalent power loss (for a given MIMO capacity) due to non-perfect total efficiencies and non-zero correlation. Hence, it can be seen as a multi-antenna extension of the single-port total efficiency

concept. For a high signal-to-noise ratio (required for MIMO multiplexing transmission) and the reference channel with uniform 3D angular power spectrum, the multiplexing efficiency for a M-port MIMO antenna is given by the compact form [27]

$$\eta_{\text{mux}} = (\prod_{k=1}^{M} \eta_k)^{1/M} \det(\mathbf{R})^{1/M} \qquad (1)$$

where η_k is the total efficiency of port k, $\mathbf{R}$ is the correlation matrix, det(.) is the determinant operator and $\prod$ is the product operator. $\mathbf{R}$ for a tri-port antenna is

$$\mathbf{R} = \begin{bmatrix} 1 & \rho_{12} & \rho_{13} \\ \rho_{12}^* & 1 & \rho_{23} \\ \rho_{13}^* & \rho_{23}^* & 1 \end{bmatrix}, \qquad (2)$$

and ρ_{mn} is the complex correlation coefficient of the far-field patterns for ports m and n [27]. For the proposed antenna, the minimum η_{mux} is calculated to be 67.0% (-1.74 dB) in the common bandwidth. Based on (1), the contributions from antenna efficiencies and correlations to η_{mux} are -1.37 dB and -0.37 dB, respectively, indicating that the efficiency dominates and the ECC values are low enough to not have any major impact on the MIMO performance.

V. PRACTICAL APPLICATIONS OF PROPOSED TRI-PORT ANTENNA

One important practical issue for terminal antennas is the effect of the big display screen, which is utilized in an opportunistic manner in this work to form a new antenna port. In this section, three other practical issues affecting terminal antennas are briefly investigated.

Firstly, the performance of the proposed tri-port antenna is studied for two typical user scenarios, i.e., one-hand (OH) data mode (see Fig. 14(a)) and two-hand (TH) mode (see Fig. 15) [28]. In these scenarios, the prototype is confined to a bounding box of dimensions 151×76×9 mm³, to account for a 0.5mm-thick casing. The simulated S parameters for OH mode (see Fig. 14(a)) show that the proposed antenna covers the same bandwidth as the free space case (see Fig. 11), but with better impedance matching for P_1. However, P_2 covers 4% less bandwidth (0.81-0.93 GHz) due to hand loading. The performance of P_2 is more affected by the hand than P_1, as the palm and fingers were positioned close to the two feeds of P_2 (i.e. $P_{2\text{-}1}$ and $P_{2\text{-}2}$) at the metal strips, affecting the near-field radiation of $P_{2\text{-}1}$ and $P_{2\text{-}2}$. Moreover, the unbalanced hand loading effect on $P_{2\text{-}1}$ and $P_{2\text{-}2}$, which are equipped with the same matching network, leads to higher mismatch. In contrast, P_1 provides more distributed nearfields between the entire chassis and screen for the monopole mode and zero near-field in the center for the patch mode, resulting in the smaller hand effect. Similarly, P_3 is positioned further away from the hand and its nearfields are strongest at the top part of the longer edges, which is less affected by the hand. The hand also marginally affects the isolation between the three ports. However, the isolation remains above 15 dB in all cases.
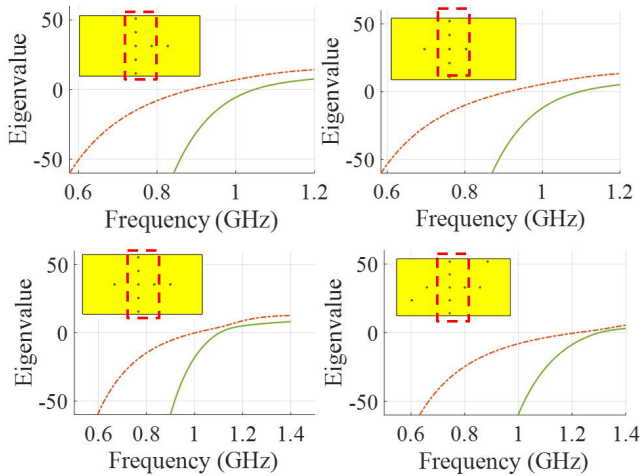
Fig. 15. Different number of shorting pins added in random locations between the chassis and screen. The red dashed rectangle is showing the original pins we used in the Fig. 1(b).

Concerning efficiency, P_1 and P_2 suffer from slightly higher absorption loss than P_3 due to the position of the feed with respect to the hand, leading to lower radiation efficiency. The average total efficiencies of the P_1, P_2, and P_3 in their operating bands are 47%, 40%, and 50%, respectively. The decrease in average total efficiency is mainly due to the radiation efficiency drops of 2.4 dB, 2.7 dB and 2.17 dB, respectively.

In the TH mode, similar to the OH mode, the simulated S parameters (see Fig. 15) show that the proposed antenna can cover the same bandwidth as the free space case, but with better impedance matching for P_1 and P_3. In the TH case, the palm is closer to the P_3, whereas in the OH scenario, the palm is closer to either the P_{2-1} or P_{2-2}. Thus, compared with the free space scenario, it can be expected that the resonance of the P_2 is slightly less influenced in the TH case, and that of the P_3 is more affected by the TH case, as has been verified in Fig. 15. P_1 is also more affected in the TH mode than the OH mode, due to the loading effect on the two ends of the handset, which has non-zero nearfield for the monopole and patch modes. In general, the port isolation between the antennas becomes higher as compared with the free space scenario, due to the high absorption loss in the hand tissue. The average total efficiencies of the P_1, P_2, and P_3 in their operating bands are 23%, 22%, and 32%, respectively. The decrease in average total efficiency is mainly due to the radiation efficiency drops of 5.8 dB, 4.2 dB and 4.6 dB, respectively.

The slightly higher ECC in Fig. 13 for the OH and TH scenarios are due to the hand impairing efficient excitation of the inherently orthogonal modes as well as the shadowing of the hand causing the far-field patterns to be more alike. However, the simulated far-field ECC is still lower than 0.14 in all cases. The peak specific absorption rate (SAR) values for both OH and TH modes were also simulated for each of the three ports in CST 2018. All the SAR values are below 2 W/kg, implying compliance with the ICNIRP guidelines for hand-only modes [29].

In the second scenario, since in practice the space between the two connected plates in Fig. 1(b) is populated with metallic components of different sizes (e.g., battery),

the impact of these objects (see Fig. 14(c)) was investigated in simulation. It was found that the metallic objects do not have much influence on the operation of the antennas and the introduced modes (CM_1-CM_4) still exist. However, as the number of objects between the plates is increased, the resonant frequencies of the CM_3 and CM_4 tend to decrease. The resonant frequencies of these modes can be re-tuned using d_2 and d_3. The operating band of P_1 and P_3 is not significantly affected, whereas P_2 experiences a small mismatch near the upper band edge due to unbalanced loading effect of the battery on the T-strip ports (i.e., P_{2-1}, P_{2-2}). However, by reoptimizing the matching component values, the matching can be restored to the desired level. ECC results are less than 0.1 in the operating band, which shows that the orthogonality of the ports is retained.

The third scenario considers electrical connections and grounding between the PCB and the screen, used to suppress unwanted radiation. These connections were modelled using several shorting pins placed at different positions (Fig. 15). It can be seen in Fig. 15 that the CM_3 and CM_4 still exists and can be excited, however, these pins tend to increase the resonant frequencies of CM_3 and CM_4, the extent to which is determined by the modal electric near-fields at the pin positions (see Fig. 2). Therefore, the modes can be retuned by optimizing the number/locations of the pins, including the pins introduced in the initial design (see Fig. 1(b)). If required, a further decrease in the resonances of both modes can be achieved by slightly increasing the chassis length (either physically or electrically by using capacitive loading at one chassis end).

VI. CONCLUSION

Based on new modes introduced by the large metal-covered screen, a tri-port MIMO antenna is proposed for the first time for large-screen smartphones, to cover cellular bands below 1 GHz. The proposed antenna is implemented without any decoupling structure and with the spacing between the feeding locations limited to half the chassis length. The strategy of identifying and selectively exciting available modes facilitates high total efficiencies (above 70%) and low ECC (below 0.16) within the operating bandwidth.

REFERENCES

[1] L. Sun, H. Feng, Y. Li, and Z. Zhang, "Compact 5G MIMO mobile phone antennas with tightly arranged orthogonal-mode pairs," *IEEE Trans. Antennas Propag.*, vol. 66, no. 11, pp. 6364–6369, Nov. 2018.

[2] J. Guo, L. Cui, C. Li, and B. Sun, "Side-edge frame printed eight-port dual-band antenna array for 5G smartphone applications," *IEEE Trans. Antennas Propag.*, vol. 66, no. 12, pp. 7412–7417, Dec. 2018.

[3] M. Abdullah, S. Kiani, and A. Iqbal. "Eight element multiple-input multiple-output (MIMO) antenna for 5G mobile applications," *IEEE Access*, vol. 7, pp. 134488-134495, 2019.

[4] H. Li, Y. Tan, B. K. Lau, Z. Ying, and S. He, "Characteristic mode based tradeoff analysis of antenna-chassis interactions for multiple antenna terminals," *IEEE Trans. Antennas Propag.*, vol. 60, no. 2, pp.409–502, Feb. 2012.

[5] S. Zhang, K. Zhao, Z. Ying, and S. He, "Adaptive quad-element multi wideband antenna array for user-effective LTE MIMO mobile terminals," *IEEE Trans. Antennas Propag.*, vol. 61, no. 8, pp. 4275–4283, Aug. 2013.

[6] H. Li, B. K. Lau, Z. Ying, and S. He, "Decoupling of multiple antennas in terminals with chassis excitation using polarization

diversity, angle diversity and current control," *IEEE Trans. Antennas Propag.*, vol. 60, no. 12, pp. 5947-5957, Dec. 2012.

[7] H. Li, Z. Miers, and B. K. Lau, "Design of orthogonal MIMO handset antennas based on characteristic mode manipulation at frequency bands below 1 GHz," *IEEE Trans. Antennas Propag.*, vol. 62, no. 5, pp. 2756–2766, May 2014.

[8] Z. Miers, H. Li, and B. K. Lau, "Design of bandwidth enhanced and multiband MIMO antennas using characteristic modes," *IEEE Antennas Wireless Propag. Lett.*, vol. 12, pp. 1696–1699, Nov. 2013.

[9] K. K. Kishor, and S. V. Hum, "Multiport multiband chassis-mode antenna design using characteristic modes," *IEEE Antennas Wireless Propag. Lett.*, vol. 16, pp. 609-612, 2017.

[10] I. Barani, and K. Wong, "Integrated inverted-F and open-slot antennas in the metal-framed smartphone for 2 x 2 LTE LB and 4 x4 LTE M/HB MIMO operations," *IEEE Trans. Antennas Propag.*, vol. 66, no. 10, pp. 5004–5012, Oct. 2018.

[11] D. Huang, Z. Du, and Y. Wang, "A quad-antenna system for 4G/5G/GPS metal frame mobile phones." *IEEE Antennas and Wireless Propag. Lett.*, vol. 18, pp. 1586-1590, 2019.

[12] S. Wang and Z. Du, "Decoupled dual-antenna system using crossed neutralization lines for LTE/WWAN smartphone applications," *IEEE Antennas Wireless Propag. Lett.*, vol. 14, pp. 523–526, 2015.

[13] H. Aliakbari and B. K. Lau. "Low-profile two-port MIMO terminal antenna for low LTE bands with wideband multimodal excitation," *IEEE Open J. Antennas Propag.*, vol. 1, pp. 368-378, 2020.

[14] J. Callaham, "The race to 100 percent: Smartphone screen-to body ratios over the years." [Online]. Available: https://www.android authority.com/smartphone-screen-to-bodyratio-878835/.

[15] "Specifications | Samsung Galaxy S9 and S9+," The Official Samsung Galaxy Site. [Online]. Available: https://www.samsung.com /global/ galaxy/galaxy-s9/specs/.

[16] B. Xiao, H. Wong, B. Wang, and K. L. Yeung, "Effect of the screen to metal-frame smartphone antennas," *IEEE Int. Workshop Antenna Technol. (iWAT)*, Miami, FL, Mar. 3-6, 2019, pp. 29-32.

[17] K. Payandehjoo, and R. Abhari, "Compact multi-band PIFAs on a semi-populated mobile handset with tunable isolation," *IEEE Trans. Antennas Propag.*, vol. 61, no. 9, pp. 4814-4819, Sep. 2013.

[18] B. Xiao, H. Wong, D. Wu, and K. L. Yeung, "Metal-frame antenna for big-screen smartphones using characteristic mode analysis," *IEEE Access*, vol. 7, pp. 122224-122231, 2019.

[19] R. Harrington and J. Mautz, "Theory of characteristic modes for conducting bodies," *IEEE Trans. Antennas Propag.*, vol. AP-19, no. 5, pp. 622–628, Sep. 1971.

[20] J. Liu, Q. Xue, H. Wong, H. W. Lai, and Y. L. Long, "Design and analysis of a low-profile and broadband microstrip monopolar patch antenna," *IEEE Trans. Antennas Propag.*, vol. 61, no. 1, pp. 11–18, Jan. 2013.

[21] J. Villanen, J. Ollikainen, O. Kivekäs, and P. Vainikainen, "Coupling element based mobile terminal antenna structures," *IEEE Trans. Antennas Propag.*, vol. 54, no. 7, pp. 2142–2153, Jul. 2006.

[22] Betamatch, version 3.7.6. (2019). MNW Scan Pte Ltd. Accessed: Mar. 16, 2020. [Online]. Available: http://www.mnw-scan.com/.

[23] H. Aliakbari and B. K. Lau, "On modal excitation using capacitive coupling elements and matching network," *in Proc. IEEE Int. Symp. Antennas Propag. (APS'2019)*, Atlanta, GA, Jul. 7-12, 2019.

[24] Satimo Stargate, Measurement System. (2010). [Online]. Available: http://www.satimo.com

[25] M. B. Knudsen and G. F. Pedersen, "Spherical outdoor to indoor power spectrum model at the mobile terminal," *IEEE J. Sel. Areas Commun.*, vol. 20, no. 6, pp. 1156–1168, Aug. 2002.

[26] R. Vaughan and J. Bach Andersen, *Channels, Propagation and Antennas for Mobile Communications*. London, U.K.: Inst. Elect. Eng., 2003.

[27] R. Tian, B. K. Lau, and Z. Ying, "Multiplexing efficiency of MIMO antennas," *IEEE Antennas Wireless Propag. Lett.*, vol. 10, pp. 183–186, 2011.

[28] H. Li, S. Sun, W. Li, M. Wu, and C. Zhou, "Systematic pattern synthesis for single antennas using characteristic mode analysis," *IEEE Trans. Antennas Propag.,* vol. 68, no. 7, pp. 5199–5208, 2020.

[29] ICNIRP Guidelines, "Guidelines for limiting exposure to time-varying electric, magnetic, and electromagnetic fields (up to 300 GHz)," *Health Phys.*, vol. 74, no. 4, pp. 494–522.